



NRC Publications Archive Archives des publications du CNRC

In situ X-ray absorption study of a layered manganese-chromium oxide-based cathode material

Balasubramanian, M.; McBreen, J.; Davidson, Isobel; Whitfield, P. S.; Kargina, I.

This publication could be one of several versions: author's original, accepted manuscript or the publisher's version. / La version de cette publication peut être l'une des suivantes : la version prépublication de l'auteur, la version acceptée du manuscrit ou la version de l'éditeur.

For the publisher's version, please access the DOI link below. / Pour consulter la version de l'éditeur, utilisez le lien DOI ci-dessous.

Publisher's version / Version de l'éditeur:

<https://doi.org/10.1149/1.1431962>

Journal of the Electrochemical Society, 149, 2, 2002

NRC Publications Record / Notice d'Archives des publications de CNRC:

<https://nrc-publications.canada.ca/eng/view/object/?id=2da01f75-3983-4cb3-b34e-086b24f0d350>

<https://publications-cnrc.canada.ca/fra/voir/objet/?id=2da01f75-3983-4cb3-b34e-086b24f0d350>

Access and use of this website and the material on it are subject to the Terms and Conditions set forth at

<https://nrc-publications.canada.ca/eng/copyright>

READ THESE TERMS AND CONDITIONS CAREFULLY BEFORE USING THIS WEBSITE.

L'accès à ce site Web et l'utilisation de son contenu sont assujettis aux conditions présentées dans le site

<https://publications-cnrc.canada.ca/fra/droits>

LISEZ CES CONDITIONS ATTENTIVEMENT AVANT D'UTILISER CE SITE WEB.

Questions? Contact the NRC Publications Archive team at

PublicationsArchive-ArchivesPublications@nrc-cnrc.gc.ca. If you wish to email the authors directly, please see the first page of the publication for their contact information.

Vous avez des questions? Nous pouvons vous aider. Pour communiquer directement avec un auteur, consultez la première page de la revue dans laquelle son article a été publié afin de trouver ses coordonnées. Si vous n'arrivez pas à les repérer, communiquez avec nous à PublicationsArchive-ArchivesPublications@nrc-cnrc.gc.ca.





In Situ X-Ray Absorption Study of a Layered Manganese-Chromium Oxide-Based Cathode Material

M. Balasubramanian,^{a,*} J. McBreen,^{a,**} I. J. Davidson,^{b,*}
P. S. Whitfield,^{b,*} and I. Kargina

^aBrookhaven National Laboratory, Materials and Chemical Sciences Division,
Department of Energy Sciences and Technology, Upton, New York 11973, USA

^bInstitute for Chemical Process and Environmental Technology, National Research Council Canada,
Ottawa, Ontario, Canada

We have investigated the electronic and atomic structure of a manganese-chromium-based layered oxide material $\text{Li}[\text{Li}_{0.2}\text{Cr}_{0.4}\text{Mn}_{0.4}]\text{O}_2$ during electrochemical cycling using *in situ* X-ray absorption spectroscopy. Our results indicate that charge compensation in the cathode material is achieved by the oxidation/reduction of octahedral Cr(III) ions to tetrahedral Cr(VI) ions during delithiation/lithiation. Manganese ions are present predominantly in the Mn(IV) oxidation state and do not appear to actively participate in the charge compensation process. To accommodate the large changes in coordination symmetry of the Cr(III) and Cr(VI) ions, the chromium ions have to move between the regular octahedral sites in the *R3m*-like lattice to interstitial tetrahedral sites during the charge/discharge process. The highly reversible (at least after the first charge) three-electron oxidation/reductions and the easy mobility of the chromium between octahedral and tetrahedral sites are very unusual and interesting. Equally interesting is the fact that chromium is the active metal undergoing oxidation/reduction rather than manganese. Our results also suggest that in the local scale manganese and chromium ions are not evenly distributed in the as-prepared material, but are present in separate domains of Mn and Cr-rich regions.

© 2002 The Electrochemical Society. [DOI: 10.1149/1.1431962] All rights reserved.

Manuscript submitted May 21, 2001; revised manuscript received September 24, 2001. Available electronically January 7, 2002.

Recently, rechargeable batteries with high energy and power density are in great demand as energy sources for various purposes; e.g., portable telecommunication, computer equipment, hybrid electric vehicles, etc. Rechargeable lithium batteries are the most promising candidates to fulfill such needs due to their intrinsic high discharge voltage and relatively light weight. The current commercial lithium-ion battery is based on a LiCoO_2 cathode and a graphitized anode. LiCoO_2 is an excellent cathode material, with good capacity, reversibility, and rate capability. However, due to the high cost and relative toxicity of Co there has been considerable interest in developing cathode materials based on Mn, V, or Ni.

Manganese-based systems offer significant cost savings, but stabilizing layered structures is hampered by the Jahn-Teller distortion exhibited by Mn(III). Layered LiMnO_2 can be synthesized,¹ but it is metastable and transforms to the cubic LiMn_2O_4 spinel on cycling. The cycling of layered LiMnO_2 can theoretically be stabilized by a number of cation substitutions,² but the ones that have received the most attention are aluminum^{3,4} and chromium.^{5,6} Challenges remain in developing a manganese-based system that can equal or beat LiCoO_2 in terms of capacity, fade, and rate capability.

Recently, it has been shown that substitution of lithium for up to about 20% of the transition metal atoms in $\text{LiCr}_y\text{Mn}_{1-y}\text{O}_2$ -type materials improves the electrochemical characteristics.^{7,8} The layered structures in $\text{Li}[\text{Li}_x\text{Cr}_y\text{Mn}_{1-x-y}]\text{O}_2$ phases are stabilized by the partial or complete oxidation of the manganese to the +4 oxidation state. In this study the changes in the atomic and electronic structure of these quaternary oxides as a function of the state-of-charge were explored by *in situ* X-ray absorption spectroscopy (XAS).

Experimental

$\text{Li}[\text{Li}_{0.2}\text{Cr}_{0.4}\text{Mn}_{0.4}]\text{O}_2$ was prepared by reacting stoichiometric quantities of a coprecipitated double hydroxide of chromium and manganese with lithium hydroxide at 800°C for 8 h under flowing argon. The chemical composition was confirmed by atomic absorption analysis. A slurry containing active material, Super S carbon black, Lonza EK15 graphite, and Kynar Flex 2801 binder in a weight ratio of 76:8.3:8.3:7.4 in *n*-methylpyrrolidinone was cast by

the doctor blade method onto aluminum foil. The cast was thoroughly dried in a convection oven held at 60°C for 24 h. Disks of 0.82 in. diam punched from the cast formed the actual cathodes.

The cathodes were incorporated into a cell with a Li foil anode, a Celgard separator, and a 1 M LiPF_6 electrolyte in a 1:1 ethyl carbonate:dimethyl carbonate (EC:DMC) solvent (LP 30 from EM Industries, Inc.). Current collection from the cathode and anode was made using thin strips of aluminum and copper, respectively. Mylar windows were used in the cell. The cell was assembled in an argon-filled glove box and was hermetically sealed prior to the measurements. The detailed design of the spectroelectrochemical cell used in the *in situ* XAS measurement is described elsewhere.⁹

The XAS experiments were performed on Beam Line X11A of the National Synchrotron Light Source (NSLS). A pair of Si(111) crystals was used to monochromatize the radiation. Harmonic contamination was suppressed by detuning the monochromator to reduce the incident X-ray intensity by ~50%. XAS scans covering both the Cr and Mn K-edges were taken in the transmission mode while charging the cell. The incident and transmitted X-ray intensities were monitored using ionization chambers filled with a mixture of helium and nitrogen gases. A third ionization chamber was used in conjunction with a Mn standard to provide internal calibration for the alignment of the edge positions.

The data were analyzed to obtain the extended X-ray absorption fine structure (EXAFS) function $\chi(k)$ using established procedures.¹⁰ The background below the edge jump was subtracted by a linear fit through the pre-edge region and extrapolated to the EXAFS region. The postedge background was determined using cubic spline procedures, which minimized the amplitude of nonphysical peaks located in the low-*r* region of the Fourier transform (FT). The EXAFS data were then normalized to a per-atom basis by dividing through the edge step height. The normalized EXAFS spectra were converted from energy to wave-vector *k* and weighted by k^3 . The data were then Fourier transformed from *k*-space to *r*-space. The FTs are shown uncorrected for the photoelectron phase shifts; thus, distances are ~0.3 to 0.4 Å shorter than actual distances between the absorber and backscattering atoms. Spurious peaks in the FTs due to spectral noise and Fourier termination effects were identified by changing the *k*-limits of the FT.¹¹ EXAFS structural parameters were obtained by nonlinear least-squares analysis of the data using phase and amplitude functions generated from the FEFF 6

* Electrochemical Society Active Member.

** Electrochemical Society Fellow.

† E-mail: mbali@bnl.gov

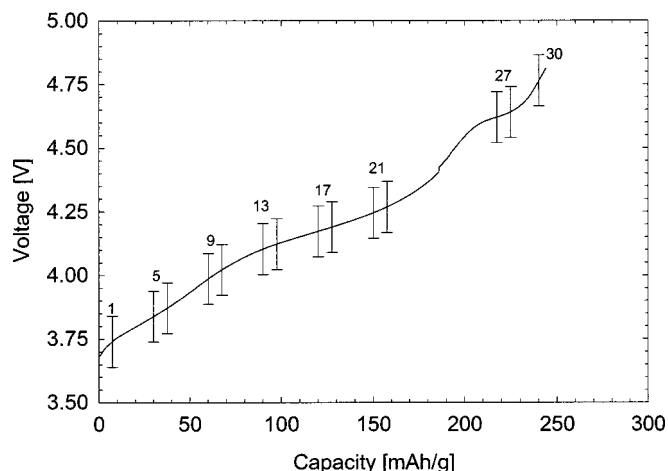


Figure 1. Voltage profile of the cell during first charge. Representative scans of the XAS measurements are indicated. The vertical marks on the curve indicate the various scan regions.

code.¹² A Gaussian distribution of bond distance was assumed in the analysis. The least-squares fits were carried out in *r*-space using FEFFIT.¹³

Results and Discussion

In situ XAS during first charge to 4.8 V.—Figure 1 shows the charging curve of a fresh cathode [18.8 mg of $\text{Li}(\text{Li}_{0.2}\text{Cr}_{0.4}\text{Mn}_{0.4})\text{O}_2$ as active material] when charged galvanostatically for ~ 13 h between 3.5 and 4.8 V. The total charge capacity was 4.58 mAh. A total of 30 scans was taken during charge. The charging was complete during the middle of scan 30. Each scan took ~ 26 min. Scan numbers, corresponding to representative XAS scans, are marked on the charging curve. The Cr edge data was collected in first half of each scan region, while the Mn edge data was collected in the second half. Thus, during the data collection time for each edge the change in Li content is $\sim 1.7\%$ of the total Li deintercalated.

Figure 2 shows the Cr K-edge XANES for representative scans taken during first charge. It can be seen that the edge position shifts

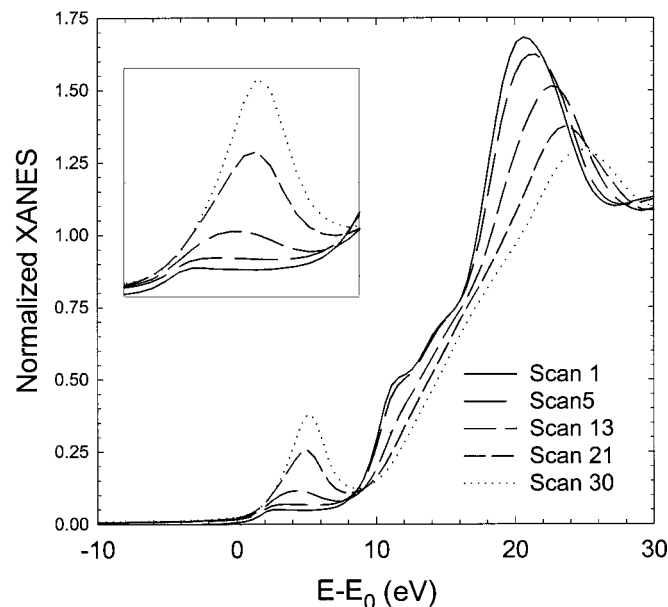


Figure 2. Cr K-edge XANES spectra during first charge. The inset shows an expanded view of the pre-edge peak region.

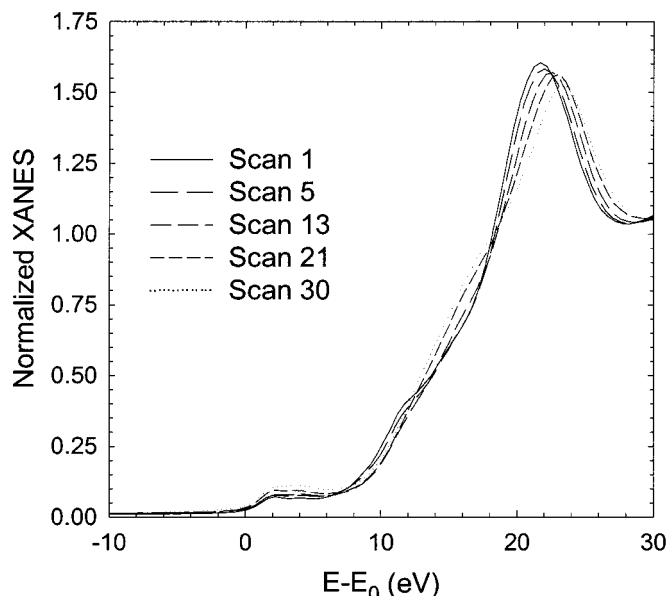


Figure 3. Mn K-edge XANES spectra during first charge.

to higher energy values as the extent of delithiation increases. Also, the shape of the overall near-edge spectra changes systematically. In particular, the pre-edge peak, shown enlarged in the inset of Fig. 2, increases in intensity as the charging progresses. In an earlier *ex situ* XAS study, Amundsen *et al.* have shown that Cr in a similar fresh cathode material is present as Cr(III) by comparing the Cr XANES with LiCrO_2 .¹⁴ The positive shift in edge position seen in Fig. 2 suggests that the average oxidation state of chromium increases on charging. In the case of Cr, in addition to the usual edge shift, spectral details in the pre-edge region provide valuable information regarding the oxidation state of the Cr absorbers. Often, Cr occurs as Cr(III) or Cr(VI) ions in its oxygen-based compounds. Cr(VI) tends to occur in tetrahedral coordination with oxygen while Cr(III) tends to occur in octahedral coordination. The XANES spectra of Cr(VI) compounds exhibit a prominent pre-edge feature that is attributed to a bound $1s \rightarrow 3d$ transition.¹⁵⁻¹⁸ This transition is forbidden in octahedral Cr(III)O_6 coordination, which has a center of inversion symmetry, but is allowed for noncentrosymmetric tetrahedral Cr(VI)O_4 coordination due to the mixing of Cr(3d) with O(2p). This mixing, in combination with the empty d-orbital ($3d^0$ configuration) of tetrahedral Cr(VI) ions, increases the probability of the $1s \rightarrow 3d$ transition, resulting in a 20-fold increase in the intensity of the pre-edge peak relative to octahedral Cr(III). The presence of significant pre-edge peak in Fig. 2 clearly indicates that Cr(III) is converted to Cr(VI) on delithiation. On the basis of the pre-edge peak intensity and using the calibration curves reported by others,¹⁶⁻¹⁸ we estimate that close to the end of charge (scan 30) $\sim 37(8)\%$ of the Cr ions in the sample are present as tetrahedral Cr(VI). Thus, a significant portion of the charge compensation can be ascribed to the oxidation of octahedral Cr(III) to Cr(VI) on delithiation.

Figure 3 shows the Mn K-edge XANES for representative scans taken during first charge. In the case of Mn, Amundsen *et al.* have earlier shown that in a similar fresh cathode material the Mn edge position coincides with that of Li_2MnO_3 , indicating that the Mn is present to a large extent as Mn(IV) in the sample.¹⁴ It can be seen in Fig. 3 that on charging the Mn edge shows some changes in the shape of the edge but does not show a rigid shift of the entire edge to higher energy values. The shape of the near-edge spectra is determined not only by the electronic structure of the Mn ion but also by backscattering processes (single as well as multiple scattering) that the ejected photoelectron undergoes during X-ray absorption.

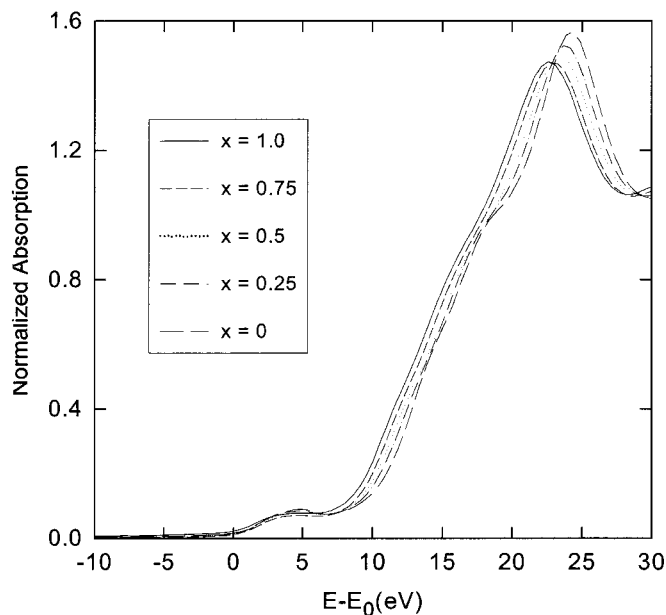


Figure 4. K-edge XANES of Mn absorbers in spinel $\text{Li}_x\text{Mn}_2\text{O}_4$ ($x = 0-1$).

For comparison, in Fig. 4 we show the *in situ* Mn XANES spectra of spinel $\text{Li}_x\text{Mn}_2\text{O}_4$ during charging in the 4 V plateau. It can be seen that the entire Mn edge shifts rigidly to higher energy values, consistent with the increase in the average oxidation state of Mn in $\text{Li}_x\text{Mn}_2\text{O}_4$. No such rigid shift is seen in the case of the Cr-Mn-based cathode material. We ascribe the changes in the shape of the Mn edge in Fig. 3 to possible rearrangement of the Mn local structure with no significant change in oxidation state of the Mn ions.

Figures 5 and 6 show representative scans of the Cr and Mn $\chi(k)$ spectra obtained during first charge. It can be seen that the Cr EXAFS changes drastically with the amplitude of the EXAFS spectra diminishing throughout the entire k -range, on charging. In contrast, the change in EXAFS spectra of the Mn absorbers is relatively small. These observations suggest that there are large local structural

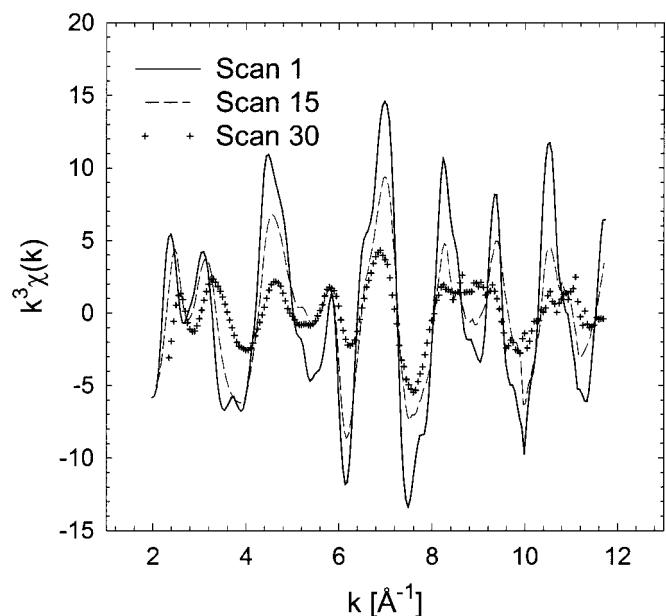


Figure 5. EXAFS $\chi(k)$ spectra for Cr absorbers during first charge.

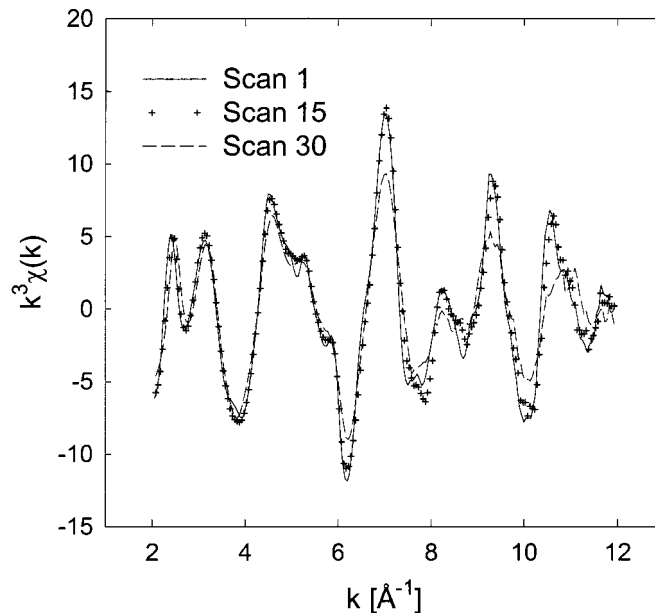


Figure 6. EXAFS $\chi(k)$ spectra for Mn absorbers during first charge.

changes around the Cr ions but only relatively minor changes around the Mn ions on delithiation. From the XANES data we know that Cr(III) is converted to Cr(VI) on charge. The Cr(VI)-O bond distance is ~ 1.65 Å in tetrahedrally coordinated Cr(VI) compounds. In contrast, the Cr(III)-O bond distance is ~ 1.98 Å in octahedrally coordinated Cr(III) compounds.¹⁵⁻¹⁸ Due to this distinct difference in the bond distances, it turns out that the electronic waves from the Cr(III)-O and Cr(VI)-O pairs (which contribute to the overall EXAFS signal) are out of phase for a significant portion of the k -range of the signal.¹⁸ This, to a large extent, accounts for the loss in Cr EXAFS amplitude on delithiation. Details of the exact nature of the cancellation of the signal can be determined by analysis of the EXAFS data.

Figures 7 and 8 show the FT of representative EXAFS scans at

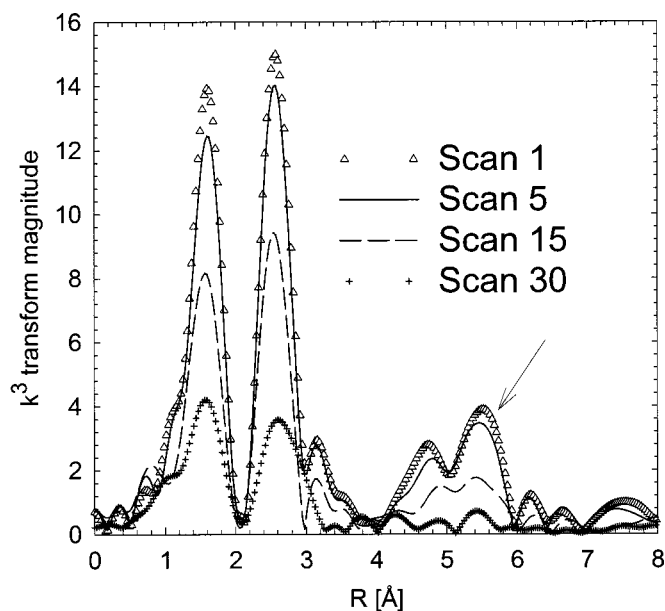


Figure 7. k^3 -weighted Fourier transform for Cr absorbers during first charge; the arrow points to the peak at ~ 5.6 Å which is ascribed to focusing effect.

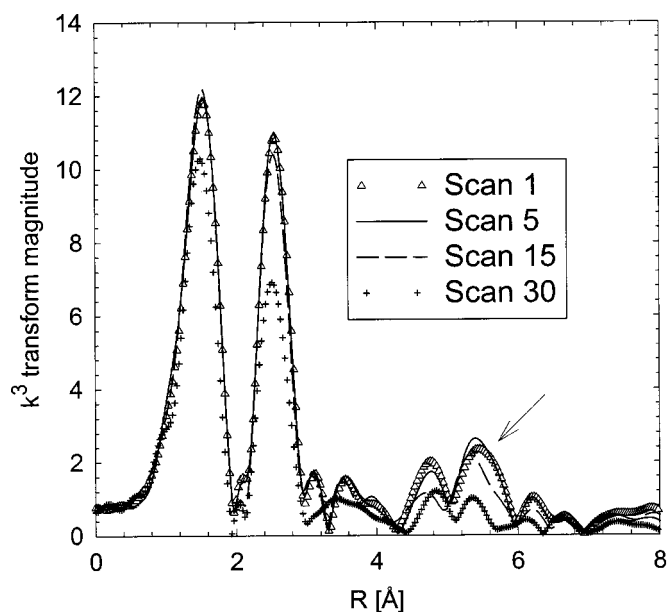


Figure 8. k^3 -weighted Fourier transform for Mn absorbers during first charge; the arrow points to the peak at ~ 5.6 Å which is ascribed to focusing effect.

the Cr and Mn edges. The first peak at ~ 1.5 Å in both the figures is due to Cr-O or Mn-O correlations. It can be seen that on delithiation the intensity of the Cr-O correlation decreases rapidly, while that of the Mn-O correlation does not change much. This reduction in the Cr-O peak intensity is due to the conversion of Cr(III) to Cr(VI) on delithiation. The second peak at ~ 2.5 Å is due to Cr-metal or Mn-metal interaction. It should be noted that as Cr and Mn are near neighbors in the periodic table, these two elements have similar backscattering properties and hence cannot be distinguished by EXAFS spectroscopy. However, the similarity in the backscattering properties allows one to use either Mn or Cr to represent the metal backscatter, without significantly affecting the EXAFS structural parameters that can be determined by detailed fits of the data. In this study the metal backscatter is represented by using Mn backscattering amplitude and phase functions.

Quantitative analysis to obtain EXAFS structural parameters of both Cr and Mn was performed by fitting the first two peaks of the FT. In the case of Cr, we find that the local structure of the fresh starting material can be well represented by six oxygen atoms at

~ 1.97 Å and six metal atoms at ~ 2.89 Å. The Cr-O bond distance of ~ 1.97 Å is consistent with what is expected for a Cr(III)-O bond. The presence of six metal atoms at ~ 2.89 Å is also in good agreement with what is expected for Cr occupying octahedral sites in the hexagonal ($R\bar{3}m$ -like) lattice.¹⁹ The Cr-metal distance corresponds well with the hexagonal “ a ” lattice parameter of 2.88 Å seen by X-ray diffraction (XRD). On charging, it can be seen from Table I that from scans 1 to 11 there is a trend showing a small reduction in the coordination number of both oxygen and metal shells. As mentioned earlier, the contribution from Cr(VI)-O and Cr(III)-O correlations would tend to cancel each other, giving rise to an apparent reduction in the coordination number of the oxygen shell. Further, Cr(VI) atoms are tetrahedrally coordinated and therefore have to move out of the regular octahedral lattice sites, creating vacancies. The presence of these vacancies leads to a reduction in the average second shell metal coordination number around Cr. The smallest splitting δR in two close-by (similar) shells that can be resolved by EXAFS is given by $\delta R \approx \pi/2k_{\max}$, where k_{\max} is maximum photoelectron wavenumber available in the experiment. In the present case, k_{\max} is ~ 12 Å⁻¹. This amounts to a spatial resolution of ~ 0.13 Å. Thus, Cr(VI)-O and Cr(III)-O bond distance can easily be resolved in the experiment. During scans 1-12 less than 10% of the Cr is oxidized to Cr(VI). This conclusion is obtained by inspecting the pre-edge peak intensity in the XANES data (Fig. 2) and by noting the reduction in the average coordination number of the Cr-O correlation. Also, due to the small amount of Cr(VI) present during scans 1-12 the EXAFS signal from the Cr(VI)-O correlations is relatively small and cannot be explicitly accounted for.

During scans 13-30 the relative amount of Cr(VI) increases and the contribution of the Cr(VI)-O bond to the EXAFS becomes clear and well defined. Therefore, for scans 13-30 the contributions from Cr in octahedral and tetrahedral sites were explicitly included. The EXAFS data is bandwidth-limited. The number of free parameters N_f that can be floated in a fit is given by $N_f \approx (2\Delta k\Delta R)/\pi$, where Δk and ΔR are the k - and R -space window widths.²⁰ Also, the information content in the EXAFS data is equally spread in R -space. Care must be taken not to utilize the free data points from neighboring peaks of the FT in determining the structural content of a given peak. Adhering to these requirements, the Cr EXAFS from scans 13-30 were modeled by fitting the first two peaks of the FT to contributions from Cr in octahedral and tetrahedral sites. In the initial fits the coordination number of the Cr-metal shell was not constrained. However, it was seen that there was a direct correlation between the number of Cr(III)-O bonds and the number of Cr-metal bonds. Further, any contribution from a possible Cr(VI)-metal correlation was negligible. This suggested that the decrease in the metal coordination number is intimately connected only with the relative

Table I. Structural parameters from nonlinear least-squares fits to the first two peaks of the Fourier transform at the Cr-edge for scans 1-12 during first charge.^a

Scan no.	Shell	N	R (Å)	σ^2 (10^{-3} Å ²)	ΔE_0 (eV)	R-factor
1	Cr-O	6.2 (1.0)	1.972 (8)	3.60 (1.56)	11.49 (1.45)	0.009
	Cr-Mn/Cr	5.7 (1.3)	2.888 (9)	4.65 (1.63)		
3	Cr-O	6.1 (1.0)	1.970 (8)	4.02 (1.64)	11.38 (1.46)	0.010
	Cr-Mn/Cr	5.5 (1.2)	2.886 (9)	4.69 (1.63)		
5	Cr-O	5.9 (1.1)	1.968 (9)	4.17 (1.81)	11.57 (1.57)	0.011
	Cr-Mn/Cr	5.5 (1.3)	2.885 (10)	4.89 (1.75)		
7	Cr-O	5.6 (1.1)	1.967 (11)	4.35 (1.95)	11.95 (1.67)	0.013
	Cr-Mn/Cr	5.6 (1.4)	2.889 (11)	5.63 (1.93)		
9	Cr-O	5.5 (1.1)	1.959 (10)	5.62 (2.00)	11.65 (1.56)	0.012
	Cr-Mn/Cr	5.4 (1.3)	2.885 (10)	5.83 (1.75)		
11	Cr-O	5.4 (1.1)	1.959 (10)	6.41 (2.23)	11.52 (1.65)	0.013
	Cr-Mn/Cr	5.4 (1.3)	2.885 (10)	6.69 (1.89)		

^a The bond distance R , disorder σ^2 , coordination number N , and inner potential shift parameter ΔE_0 are tabulated. The value of the R-factor, which is a measure of the goodness of the fit, is also tabulated. The number in the parenthesis is the uncertainty in the last digit or digits of the parameter, determined using the procedure described in Ref. 13.

Table II. Structural parameters from nonlinear least-squares fits to the first two peaks of the Fourier transform at the Cr-edge for scans 13-30 during first charge.^a

Scan no.	Shell	Cr in octahedral sites (%)	Cr in tetrahedral sites (%)	Distance (Å)	Disorder (10^{-3}Å^2)	ΔE_0 (eV)	R-factor
13	Cr(III)-O	92 (6)	8 (6)	1.945 (9)	6.99 (1.05)	11.3 (1.3)	0.011
	Cr(VI)-O			1.634 (65)	6.99 (1.05)		
15	Cr-Mn/Cr	92 (6)	13 (5)	2.884 (9)	7.56 (0.70)	11.0 (1.6)	0.009
	Cr(III)-O	87 (5)		1.940 (9)	6.88 (1.17)		
17	Cr(VI)-O	87 (5)	18 (3)	1.632 (53)	6.88 (1.17)	11.8 (1.2)	0.006
	Cr-Mn/Cr	82 (3)		1.943 (8)	7.44 (0.89)		
19	Cr(III)-O	82 (3)	21 (3)	1.637 (27)	7.44 (0.89)	12.1 (1.2)	0.006
	Cr(VI)-O	79 (3)		1.941 (8)	8.13 (0.86)		
21	Cr-Mn/Cr	79 (3)	28 (2)	1.633 (22)	8.13 (0.86)	12.4 (1.0)	0.004
	Cr(III)-O	72 (2)		2.895 (9)	9.35 (0.61)		
23	Cr(VI)-O	72 (2)	33 (3)	1.940 (6)	8.56 (0.59)	12.6 (1.4)	0.009
	Cr-Mn/Cr	67 (3)		1.630 (1)	8.56 (0.59)		
27	Cr(III)-O	67 (3)	42 (3)	2.900 (7)	9.97 (0.48)	14.2 (1.8)	0.014
	Cr(VI)-O	58 (3)		1.939 (9)	9.17 (0.88)		
30	Cr-Mn/Cr	58 (3)	43 (3)	1.623 (13)	9.17 (0.88)	14.8 (1.9)	0.015
	Cr(III)-O	57 (3)		2.902 (12)	11.3 (0.9)		
	Cr(VI)-O	57 (3)		1.953 (11)	8.03 (0.70)		
	Cr-Mn/Cr	57 (3)		1.639 (16)	8.03 (0.70)		
	Cr(III)-O	57 (3)		2.918 (9)	11.7 (1.3)		
	Cr(VI)-O	57 (3)		1.951 (11)	7.39 (0.75)		
	Cr-Mn/Cr	57 (3)		1.636 (16)	7.39 (0.75)		
				2.919 (9)	12.0 (1.2)		

^a A model based on Cr ions occupying either octahedral or tetrahedral sites was used in the analysis. The bond distance R , disorder σ^2 , inner potential shift parameter ΔE_0 , and the R-factor of the fit are tabulated. The number in the parenthesis is the uncertainty in the last digit or digits of the parameter.

amount of octahedrally coordinated Cr(III). Thus, in the final fits the coordination number of the Cr(III)-O bond and that of the Cr-metal bond were constrained to be the same. This constraint accurately accounts for the reduction in the metal coordination number due to the formation of vacancies created by the movement of Cr(VI) ions away from regular octahedral sites. In addition, to minimize the correlation between coordination number and disorder, the disorder parameter of the Cr(VI)-O and Cr(III)-O correlation were constrained to be equal. Also, a single inner potential shift parameter ΔE_0 was found to be sufficient to represent both the oxygen and metal shell of atoms.

The structural parameters that we obtained for scans 13-30 using this fitting procedure are given in Table II. A representative fit to experimental data is shown in Fig. 9. It can be seen from Table II that from scans 13 to 30 the amount of tetrahedral Cr increases from ~8 to ~43%. The presence of 43% tetrahedral Cr is also consistent with the value obtained from the XANES pre-edge peak intensity. The tetrahedral Cr-O bond distance of ~1.64 Å is in agreement with those found in Cr(VI) compounds.¹⁵⁻¹⁸ The analysis clearly shows that the reduction in the intensity of the second peak of the FT (Cr-metal correlation) on delithiation is due to the migration of Cr ions from regular octahedral sites to tetrahedral sites. It can be seen from both Tables I and II that on delithiation the disorder of Cr-O as well as Cr-metal correlations increases significantly. For scans 1-12, it is tempting to attribute this increased disorder to different bond lengths of the tetrahedral and octahedral Cr-O pairs. However, it can be seen from Table II that even after accounting for the two different sites, the structural disorder is still significantly larger than that seen for the fresh cathode material. It is conceivable that the increased disorder represents a "true" increase in the static disorder of the bonds and might be due to the strain imposed on the structure by the formation of vacancies.

Unlike the case of Cr, we found that the first two peaks in the FT of Mn can always be well represented by a single Mn-O distance and a single Mn-metal distance. The structural parameters obtained by the two-shell analysis are given in Table III. We find that for all

states of charge the first shell contains ~6 Mn-O bonds at ~1.89 Å and ~4 Mn-metal bonds at ~2.87 Å. The Mn-O distance of ~1.89 Å is in agreement with what is expected for a Mn(IV)-O bond.²¹ Also, the disorder of the Mn-O pairs is comparable to that seen around Cr in the fresh cathode material. The presence of Mn(III) would tend to increase the overall disorder of the Mn-O bond due to the large local Jahn-Teller distortion expected for Mn(III). The ab-

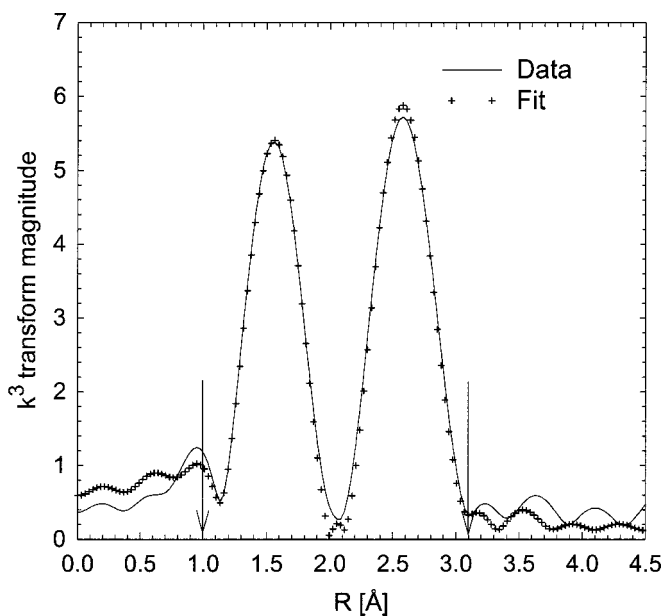


Figure 9. A representative R-space fit (scan 21) of the first two peaks of the Fourier transform for Cr absorbers during first charge. The arrows indicate the r-range over which the fit was performed.

Table III. Structural parameters from nonlinear least-squares fits to the first two peaks of the Fourier transform at the Mn-edge for scans 1-30 during first charge.^a

Scan no.	Shell	Number of neighbors	Distance (Å)	Disorder ($\times 10^{-3} \text{ \AA}^2$)	ΔE_0 (eV)	R-factor
1	Mn-O	6.1 (7)	1.894 (7)	4.55 (1.06)	10.6 (1.2)	0.005
	Mn-Mn/Cr	3.9 (7)	2.873 (7)	3.62 (1.22)		
3	Mn-O	6.0 (7)	1.892 (7)	4.19 (1.07)	10.6 (1.2)	0.005
	Mn-Mn/Cr	3.8 (7)	2.872 (8)	3.28 (1.26)		
5	Mn-O	6.3 (9)	1.891 (7)	4.81 (1.41)	10.5 (1.6)	0.008
	Mn-Mn/Cr	3.7 (9)	2.867 (7)	3.22 (1.59)		
7	Mn-O	6.1 (8)	1.891 (8)	4.46 (1.30)	10.9 (1.5)	0.008
	Mn-Mn/Cr	4.1 (9)	2.869 (9)	4.17 (1.62)		
9	Mn-O	6.1 (7)	1.890 (7)	4.20 (1.12)	10.9 (1.3)	0.006
	Mn-Mn/Cr	4.1 (8)	2.865 (8)	4.30 (1.45)		
11	Mn-O	6.2 (9)	1.893 (9)	4.43 (1.40)	11.2 (1.6)	0.009
	Mn-Mn/Cr	4.0 (9)	2.865 (10)	3.97 (1.75)		
15	Mn-O	6.2 (9)	1.887 (9)	4.53 (1.47)	10.6 (1.7)	0.01
	Mn-Mn/Cr	3.9 (1.0)	2.861 (10)	4.14 (1.80)		
17	Mn-O	6.1 (1.0)	1.889 (9)	4.82 (1.68)	10.7 (1.9)	0.013
	Mn-Mn/Cr	4.0 (1.2)	2.865 (10)	4.78 (2.24)		
19	Mn-O	6.3 (1.0)	1.886 (9)	5.67 (1.60)	10.0 (1.8)	0.011
	Mn-Mn/Cr	4.2 (1.2)	2.858 (10)	6.02 (2.19)		
21	Mn-O	5.6 (8)	1.892 (9)	4.4 (1.40)	11.2 (1.7)	0.010
	Mn-Mn/Cr	4.1 (1.2)	2.869 (10)	6.25 (2.22)		
23	Mn-O	5.6 (8)	1.892 (9)	4.4 (1.40)	11.2 (1.7)	0.010
	Mn-Mn/Cr	4.1 (1.2)	2.869 (10)	6.25 (2.22)		
27	Mn-O	5.2 (6)	1.888 (7)	5.04 (1.10)	10.6 (1.3)	0.006
	Mn-Mn/Cr	4.4 (1.0)	2.870 (7)	8.65 (2.02)		
30	Mn-O	5.3 (4)	1.879 (4)	4.69 (0.57)	9.5 (1.0)	0.002
	Mn-Mn/Cr	4.4 (6)	2.863 (6)	8.45 (1.07)		

^a The bond distance R , disorder σ^2 , coordination number N , inner potential shift parameter ΔE_0 , and the R-factor of the fit are tabulated. The number in the parenthesis is the uncertainty in the last digit or digits of the parameter.

sence of a significant increase in the disorder around Mn in the sample suggests that the amount of Mn(III), if any, is minimal. The Mn-metal correlation at $\sim 2.87 \text{ \AA}$ is consistent with the hexagonal “ a ” lattice parameter seen in XRD.¹⁹ However, note that for all states of charge there appears to be only ~ 4 Mn-metal correlations. In the case of Cr, the fresh cathode material had ~ 6 Cr-metal correlations. This reduction in Mn-metal correlation suggests that the second shell around Mn contains either vacancies or Li ions. Li is a very weak backscatter and cannot be clearly seen by EXAFS spectroscopy. As the sample is Li-rich, it is conceivable that the extra Li is clustered preferentially around the Mn atoms. Also, we point out that there is no change in the number of Mn-metal bonds on delithiation. In the case of Cr the number of Cr-metal bonds decreases significantly on delithiation (Table II). The relative step heights at the Mn and Cr K-edges confirms that the ratio of Cr to Mn in the sample is $\sim 1.00(5)$. If Cr and Mn are randomly distributed in the hexagonal lattice, each metal atom (irrespective of whether it is Mn or Cr), on an average, will be surrounded by an equal number of Cr and Mn neighbors. On delithiation, some of the Cr migrates to tetrahedral sites. This should cause a reduction in the number of metal-metal correlations around both Cr as well as Mn. However, as pointed out earlier, no reduction in the number of Mn-metal correlation is seen on delithiation. These observations strongly suggest that on a local atomic scale Cr and Mn are not randomly distributed. The sample contains separate domains of Cr and Mn-rich regions.

Additional evidence for the presence of separate Cr- and Mn-rich domains can be obtained by a careful inspection of the peaks at higher R in the FTs shown in Fig. 7 and 8. For both Cr and Mn in the fresh cathode material a peak occurs at $\sim 5.6 \text{ \AA}$ (indicated by arrows in the FTs). The intensity of this peak is much larger for Cr than for Mn. This peak is seen in several 3d transition metal oxides with hexagonal layered structure and arises from a three-body correlation (often referred to as focusing effect) involving the coherent linear chains of edge-sharing transition-metal octahedra.^{14,15,22,23} The intensity of the peak is maximum when the dihedral angle in-

involved in the probe-metal-metal bond is 180° . Deviations from colinearity due to local distortion (say, due to presence of Li in the metal sites) or broken chains (caused by vacancies) lead to a drastic reduction in the peak height. The lower intensity of the peak at $\sim 5.6 \text{ \AA}$ in the case of Mn is in accordance with the presence of Li or vacancies in the second shell of Mn. Further, it can be seen that there is a rather drastic collapse of this peak in Cr on delithiation. This collapse occurs due to the introduction of vacancies and increased disorder around the probed Cr ions on delithiation.

It can also be seen in Fig. 8 that close to the end of charge (scan 30) the intensity of the first peak is diminished. This diminution manifests itself as a reduction in the Mn-O coordination in scans close to the end of charge (Table III). Due to the correlation between disorder and coordination number it is not clear if this reduction in coordination number is a real effect or if it is just a numerical artifact of the analysis. However, we note that electrochemical measurements show that the cyclability of the material is degraded when the material is charged to voltage higher than 4.5 V (*vs.* Li). The reduced coordination number at high voltages might play a role in the poorer cyclability of the material.

In situ XAS during first discharge and second charge.—To understand the reversibility of the redox process, further *in situ* measurements were performed during first discharge and second charge. A fresh cathode (13.68 mg of $\text{Li}[\text{Li}_{0.2}\text{Cr}_{0.4}\text{Mn}_{0.4}]\text{O}_2$ as active mass) was again incorporated into the spectroelectrochemical cell, and the first charge to 4.5 V was carried out off-line at a C/12 rate. The cathode material came from a separate batch prepared in an identical manner to the first. The chemical composition was confirmed by atomic absorption analysis. After ~ 6 h of rest at a high state-of-charge, the cell was mounted on-line and the cathode was discharged to 2.5 V (first discharge). The sample was then charged again (second charge) to 4.5 V after rest at the discharged state for ~ 25 min. XAS measurements were performed during the cycling

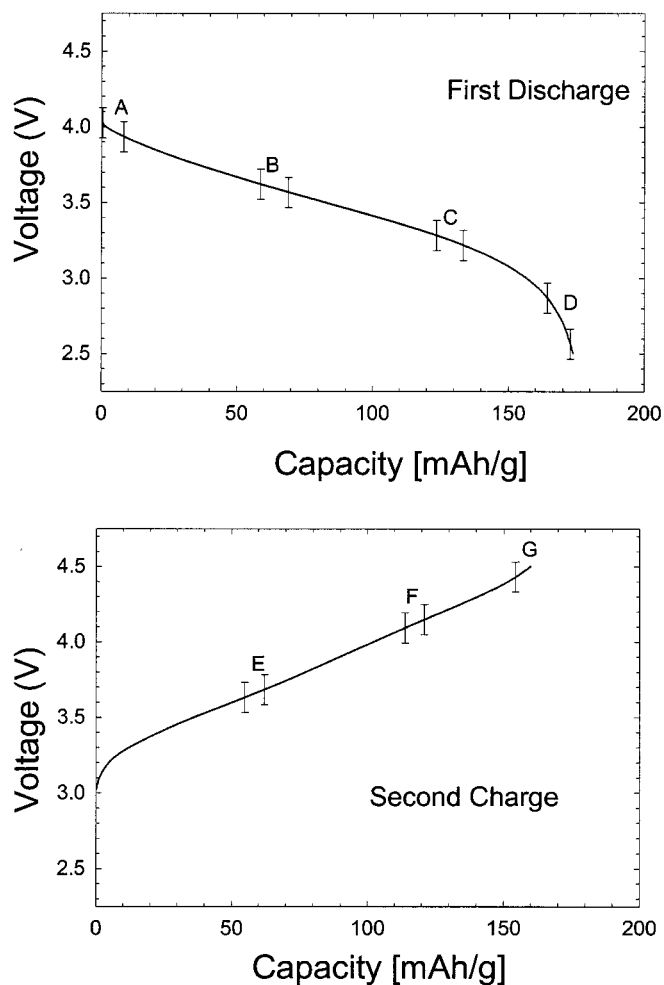


Figure 10. Voltage profile of the cell during first discharge and second charge. Representative scans of the XAS measurements are indicated. The vertical marks on the curve indicate the various scan regions.

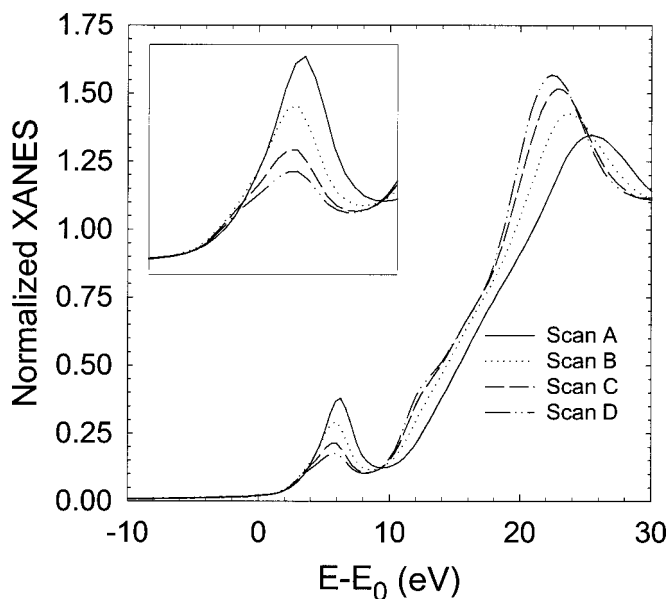


Figure 11. Cr K-edge XANES spectra during first discharge. The inset shows an expanded view of the pre-edge peak region.

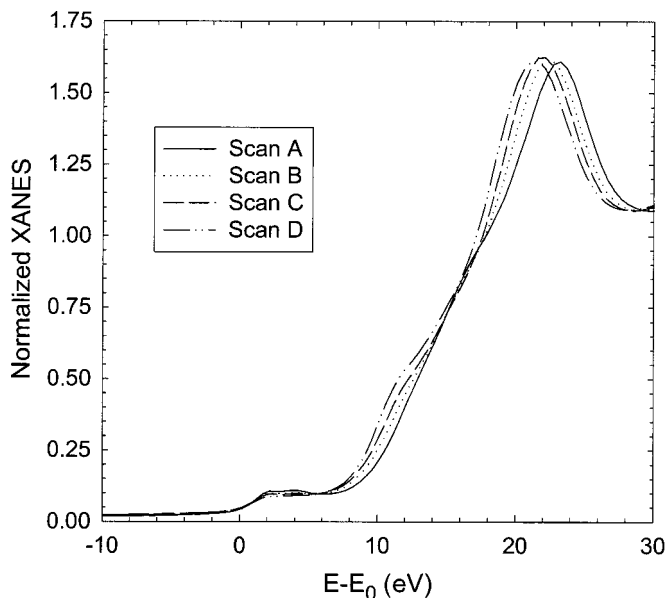


Figure 12. Mn K-edge XANES spectra during first discharge.

process. The cycling curve during first discharge and second charge is shown in Fig. 10. Representative scans are marked on the cycling curve.

Figure 11 shows the Cr XANES during the first discharge. It can be seen that at the start of discharge (scan A), a large pre-edge peak is present. This shows that significant portions of the Cr ions are present in tetrahedral sites. On discharge, the intensity of the pre-edge peak decreases progressively. This suggests that Cr(VI) is reduced to Cr(III). However, even at the end of discharge (scan D) the intensity of the pre-edge peak is not as small as what is seen for the fresh cathode material (Fig. 2). This shows that when discharged at the C/10 rate to 2.5 V, not all Cr(VI) ions are converted to Cr(III). On the basis of the pre-edge peak intensity, it appears that $\sim 15(8)\%$ Cr is still present as Cr(VI) ions.

Figure 12 shows the Mn edge XANES obtained during first discharge. As in the case of the first charge (Fig. 3), the entire edge

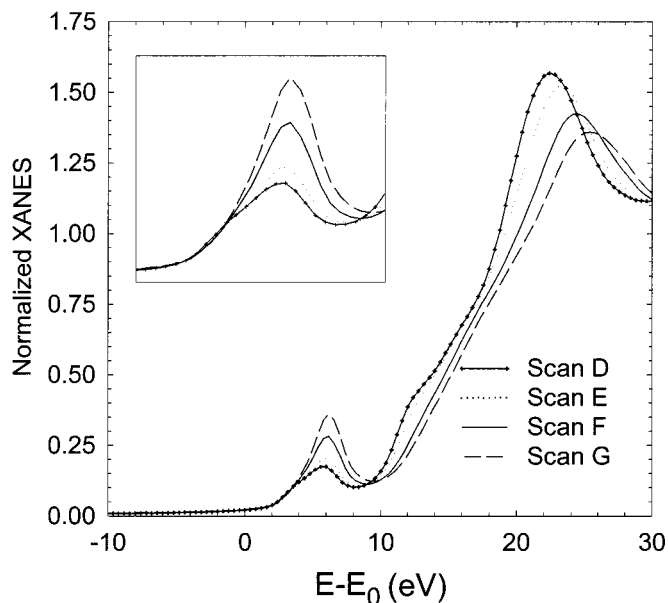


Figure 13. Cr K-edge XANES spectra during second discharge. The inset shows an expanded view of the pre-edge peak region.

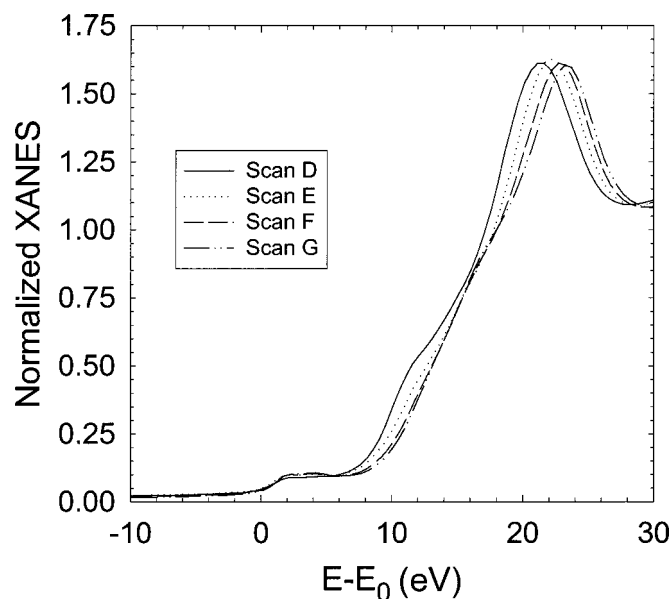


Figure 14. Mn K-edge XANES spectra during second discharge.

does not shift rigidly on lithiation. We therefore ascribe the changes in the shape of the XANES to possible local rearrangement around the Mn ions, without much change in the Mn oxidation state. However, the changes in the shape of Mn-edge between first charge and first discharge are not completely identical. This suggests that the local structural rearrangement around the Mn ions on discharge is not identical to that seen during first charge. Therefore, we come to the conclusion that the local structural changes endured during first charge are not completely reversible.

Figure 13 shows the Cr edge XANES during the second charge. It can be seen that the amount of Cr(VI) increases during the second charge as expected. At the end of the second charge, the intensity of the pre-edge peak (scan G) becomes almost the same as that found

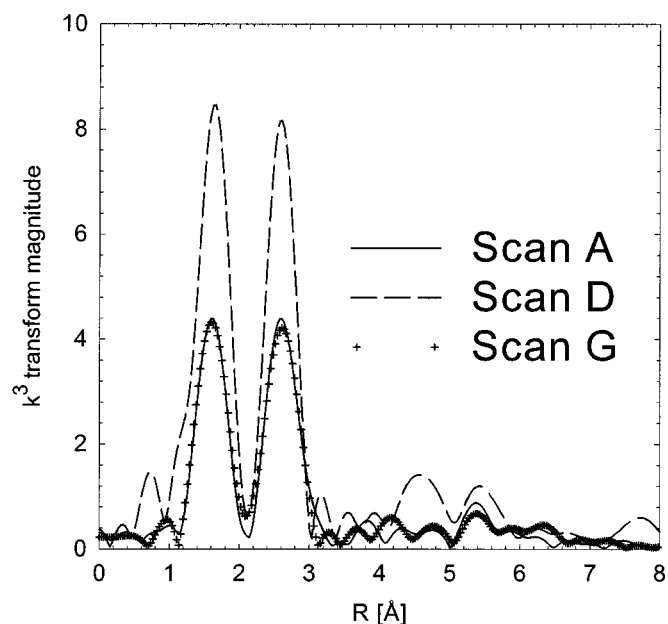


Figure 15. k^3 -weighted Fourier transform for Cr absorbers during first discharge and second charge. Three representative scans are plotted.

at the beginning of the first discharge (scan A, Fig. 11). This indicates that almost all the tetrahedral Cr(VI) that was reduced to octahedral Cr(III) during first discharge was recovered during the second charge. Thus, the redox behavior of Cr during first discharge and second charge is highly reversible. Figure 14 shows the Mn XANES taken during the second charge. It can be seen that the changes in the shape of the Mn XANES is similar to that seen during the first discharge (Fig. 12). Thus, the XANES data strongly suggests that both the redox behavior and local structural changes are highly reversible after the first charge.

Table IV. Structural parameters from nonlinear least-squares fits to the first two peaks of the Fourier transform at the Cr-edge for selected scans during first discharge and second charge.^a

Scan no.	Shell	Cr in octahedral sites (%)	Cr in tetrahedral sites (%)	R (Å)	σ^2 (10^{-3} \AA^2)	ΔE_0 (eV)	R-factor
A	Cr(III)-O	61 (2)		1.974 (8)	7.90 (0.64)	12.3 (1.4)	0.008
	Cr(VI)-O		39 (2)	1.659 (8)	7.90 (0.64)		
	Cr-Mn/Cr	61 (2)		2.929 (10)	10.7 (0.71)		
B	Cr(III)-O	73 (4)		1.981 (10)	6.67 (0.95)	10.9 (1.9)	0.013
	Cr(VI)-O		27 (4)	1.666 (20)	6.67 (0.95)		
	Cr-Mn/Cr	73 (4)		2.924 (14)	9.39 (0.94)		
C	Cr(III)-O	82 (5)		1.989 (12)	5.68 (1.28)	10.1 (2.1)	0.016
	Cr(VI)-O		18 (5)	1.705 (46)	5.68 (1.28)		
	Cr-Mn/Cr	82 (5)		2.926 (15)	8.37 (1.00)		
D	Cr(III)-O	87 (7)		1.992 (14)	5.55 (1.78)	9.9 (2.5)	0.021
	Cr(VI)-O		13 (7)	1.725 (97)	5.55 (1.78)		
	Cr-Mn/Cr	87 (7)		2.931 (18)	8.57 (1.22)		
E	Cr(III)-O	83 (6)		1.978 (12)	5.31 (1.50)	9.2 (2.2)	0.017
	Cr(VI)-O		17 (6)	1.715 (58)	5.31 (1.50)		
	Cr-Mn/Cr	83 (6)		2.915 (15)	8.00 (1.01)		
F	Cr(III)-O	75 (5)		1.972 (13)	7.67 (1.31)	10.1 (2.2)	0.018
	Cr(VI)-O		25 (5)	1.661 (28)	7.67 (1.31)		
	Cr-Mn/Cr	75 (5)		2.915 (16)	9.58 (1.09)		
G	Cr(III)-O	64 (3)		1.981 (11)	8.84 (0.99)	12.9 (1.9)	0.014
	Cr(VI)-O		36 (3)	1.655 (14)	8.84 (0.99)		
	Cr-Mn/Cr	64 (3)		2.934 (15)	11.3 (1.03)		

^a A model based on Cr ions occupying either octahedral or tetrahedral sites was used in the analysis. The bond distance R , disorder σ^2 , inner potential shift parameter ΔE_0 , and R-factor are tabulated. The number in the parenthesis is the uncertainty in the last digit or digits of the parameter.

The findings of the EXAFS data analysis are also in agreement with the results of the XANES data. The Mn EXAFS data taken during first discharge and second charge shows that for all states of charge Mn ions are surrounded by *ca.* six oxygen and four metal neighbors. Apart from a slight increase in the disorder, the structural parameters obtained for the Mn data during the first discharge and second charge are very similar to that seen during first charge (Table III). In contrast to the Mn EXAFS, the Cr-edge EXAFS shows large changes (consistent with redox behavior of Cr ions in this system). Figure 15 shows the FT of Cr EXAFS taken during the first discharge and second charge. It can be seen that at the start of the first discharge (scan A), the peak height of both the Cr-O and Cr-metal interactions are small as expected. At the end of discharge (scan D), the intensity of the peaks representing the Cr-O interaction as well as the Cr-metal interaction increases significantly. This suggests that the Cr(VI) ions on reduction to Cr(III) migrate back to regular octahedral sites on the $R\bar{3}m$ -like lattice. It is remarkable that the Cr ions can move back and forth between octahedral and tetrahedral sites during the charge/discharge process. The remarkable nature of the redox process is further exemplified during the second charge. Close to the end of the second charge the peak heights of the Cr-O and Cr-metal interactions (scan G) again diminish, consistent with the movement of Cr ions from octahedral to tetrahedral sites. Table IV shows the structural parameters obtained by the analysis of the EXAFS data during first discharge and second charge. It can be seen that at the start of first discharge $\sim 39(2)\%$ of Cr occupies tetrahedral sites. At the end of first discharge, the amount of tetrahedral Cr(VI) ions decreases. However, note that a fraction of Cr ions [$\sim 13(7)\%$] are still in the Cr(VI) state. This is consistent with the results of the Cr XANES spectra. At the end of second charge, $\sim 36(3)\%$ of the Cr again occupies tetrahedral sites as Cr(VI) ions; similar to that seen at the start of first discharge. This indicates that the redox behavior and local structural changes during the first discharge and second charge are highly reversible.

Conclusion

We have investigated the evolution of the local electronic and atomic structure of a Mn-Cr-based layered cathode material using *in situ* Cr and Mn K-edge XAS measurements during electrochemical delithiation/lithiation. We have measured the changes in the coordination numbers, bond distances, and local disorder as a function of the state-of-charge of the material. The XAS measurements show that during the first charge, charge compensation is largely achieved by the conversion of Cr(III) to Cr(VI). This conversion leads to the migration of Cr from regular octahedral sites in the $R\bar{3}m$ -like lattice to tetrahedral sites, leaving behind vacancies at the octahedral sites. In strong contrast, apart from a possible subtle local rearrangement of the structure, Mn ions do not seem to actively participate in the charge compensation. Our results also indicate that on a local scale separate domains of Cr- and Mn-rich regions are present in the material. Further, the excess Li ions (in the fresh cathode material) appear to be clustered preferentially about Mn.

During the first discharge, most of the Cr(VI) ions are reduced to Cr(III). However, a small amount of Cr(VI) is present even after discharge to 2.5 V (at $\sim C/10$ rate). Our Cr and Mn XAS results show that the structural changes associated with the first charge are not completely reversed during first discharge. During the second charge, changes in the local structure and oxidation states of the transition metal atoms are in accordance with the results found during first discharge. At the end of the second charge, the amount of Cr(VI) present in the sample is almost identical to that found at the beginning of the first discharge. These results indicate that changes

in the structure are much more reversible after the first charge.

The finding that Cr, to a large extent, is the active metal undergoing oxidation/reduction rather than Mn is very interesting and unusual. Equally interesting are the high reversibility (at least after first charge) of the three-electron oxidation/reduction process and the unhindered mobility of Cr between octahedral and tetrahedral sites. The element-specific nature of the XAS technique and its sensitivity to two and three-body correlations make it an ideal tool to complement the results of conventional diffraction techniques. The value of local probes (such as XAS) in obtaining structural and electronic information, on such complex and important materials, is aptly demonstrated by this study.

Acknowledgments

The authors thank Steven Argue and Yves Grincourt for the chemical analyses and preparation of the electrodes, respectively. The XAS work was supported by the Assistant Secretary for Energy Efficiency and Renewable Energy, Office of Advanced Automotive Technologies, and the Division of Materials Science, Office of Science, U.S. Department of Energy (DOE) under contract no. DE-AC02-98CH10886. The work was done under the auspices of the Batteries for Advanced Transportation Technologies Program.

Brookhaven National Laboratory assisted in meeting the publication costs of this article.

References

1. A. R. Armstrong and P. G. Bruce, *Nature*, **381**, 499 (1999).
2. G. Ceder and S. K. Mishra, *Electrochem. Solid-State Lett.*, **2**, 550 (1999).
3. Y.-I. Jang, B. Huang, Y.-M. Chiang, and D. R. Sadoway, *Electrochem. Solid-State Lett.*, **1**, 13 (1998).
4. Y.-M. Chiang, D. R. Sadoway, Y.-I. Jang, B. Huang, and H. Wang, *Electrochem. Solid-State Lett.*, **2**, 107 (1999).
5. I. J. Davidson, R. S. McMillan, H. Slegel, B. Luan, I. Kargina, J. J. Murray, and I. P. Swainson, *J. Power Sources*, **81-82**, 406 (1998).
6. J. R. Dahn, T. Zheng, and C. L. Thomas, *J. Electrochem. Soc.*, **145**, 851 (1998).
7. C. Storey, I. Kargina, Y. Grincourt, I. J. Davidson, Y. Yoo, and D. Y. Seung, Abstract 234, 10th International Meeting on Lithium Batteries, Como, Italy, May 28-June 2, 2000.
8. J. Cho and B. Park, *Electrochem. Solid-State Lett.*, **3**, 355 (2000).
9. M. Balasubramanian, X. Sun, X. Q. Yang, and J. McBreen, *J. Power Sources*, **92**, 1 (2001).
10. D. E. Sayers and B. A. Bunker, *X-Ray Absorption: Principles, Application, Techniques of EXAFS, SEXAFS and XANES*, Chap. 6, D. C. Koningsberger and R. Prins, Editors, Wiley, New York (1988).
11. F. W. Lytle, *Applications of Synchrotron Radiation*, Gordon and Breach, New York (1989).
12. S. I. Zabinsky, J. J. Rehr, A. Ankudinov, and M. J. Eller, *Phys. Rev. B*, **52**, 2995 (1995).
13. E. A. Stern, M. Newville, B. Ravel, Y. Yacoby, and D. Haskel, *Physica B*, **208 & 209**, 117 (1995).
14. B. Ammundsen, J. Paulsen, I. Davidson, and Ru-Shi Liu, *J. Electrochem. Soc.*, To be published.
15. M. Balasubramanian and C. A. Melendres, *J. Synchrotron Radiat.*, **6**, 594 (1999).
16. M. L. Peterson, G. E. Brown, G. A. Parks, and C. L. Stein, *Geochim. Cosmochim. Acta*, **61**, 3399 (1997).
17. A. J. Davenport, H. S. Isaacs, G. S. Frankel, A. G. Schrott, C. V. Jahnes, and M. A. Russak, *J. Electrochem. Soc.*, **138**, 338 (1991).
18. A. Manceau and L. Charlet, *J. Colloid Interface Sci.*, **148**, 425 (1992).
19. P. S. Whitfield, I. J. Davidson, I. Kargina, Y. Grincourt, B. Ammundsen, J. McBreen, and M. Balasubramanian, in *Rechargeable Lithium Batteries*, M. Doyle, E. Takeuchi, and K. M. Abraham, Editors, PV 2000-21, p. 106, The Electrochemical Society Proceedings Series, Pennington, NJ, In press.
20. E. A. Stern, *Phys. Rev. B*, **48**, 9825 (1993).
21. B. Ammundsen, D. J. Jones, J. Roziere, and F. Villain, *J. Phys. Chem. B*, **102**, 7939 (1998).
22. P. A. O'Day, J. J. Rehr, S. I. Zabinsky, and G. E. Brown, *J. Am. Chem. Soc.*, **116**, 2938 (1994).
23. K. I. Pandya, W. E. O'Grady, D. A. Corrigan, J. McBreen, and R. W. Hoffman, *J. Phys. Chem.*, **94**, 21 (1990).